Transboundary transport of non-east and East Asian dust observed at Dunhuang, northwest China

Tian Zhou [a], Xiaowen Zhou [a], Zining Yang [b], Carmen Córdoba-Jabonero [c], Yufei Wang [a], Zhongwei Huang [a,*], Pengbo Da [a], Qiju Luo [d], Zhijuan Zhang [e], Jinsen Shi [a], Jianrong Bi [a], Hocine Alikhodja [f]

[a] *Key Laboratory for Semi-Arid Climate Change of the Ministry of Education, College of Atmospheric Sciences, Lanzhou University, Lanzhou, 730000, Gansu, China*
[b] *School of Earth and Space Sciences, University of Science and Technology of China, Hefei, 230026, China*
[c] *Instituto Nacional de Técnica Aeroespacial (INTA), Atmospheric Research and Instrumentation Branch, Torrejón de Ardoz, 28850, Madrid, Spain*
[d] *LuDian Meteorological Bureau, Zhaotong, 657000, Yunnan, China*
[e] *College of Environmental Science and Engineering, Taiyuan University of Technology, Taiyuan, 030024, China*
[f] *Laboratoire de Pollution et Traitement des Eaux, Département de Chimie, Faculté des Sciences Exactes, Université Frères Mentouri-Constantine 1, Constantine, Algeria*

HIGHLIGHTS

- POLIPHON algorithm was conducted to the P-MPL observations over northwest China.
- A noticeable contrast exists in the vertical structure between the long-range transported and fresh dust plumes.
- Model underestimates the contribution of long-range transported dust to local aerosol loading.

GRAPHICAL ABSTRACT
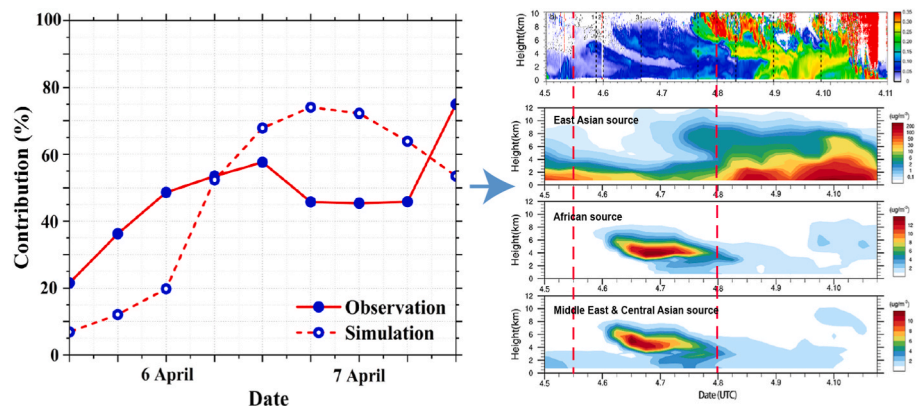
ARTICLE INFO

ABSTRACT

Long-range transport of North African and Middle Eastern dust has been frequently observed in East Asia. However, understanding of their characteristics and effects in this region is insufficient. In this study, the transboundary transport of multi-source dust was captured by a polarized micro-pulse lidar from April 5 to 10, 2012, during a field campaign in Dunhuang, northwest China. Six dust plumes (DN1-DN6) were selected based on the spatiotemporal evolution of the depolarization ratio. Furthermore, the source, vertical characteristics of the coarse and fine components and their contributions were investigated by combining lidar observation with the WRF-Chem model simulation. The results indicated that DN1 was from Central Asia and it took approximately 4–5 days. DN2 originated from sources in North Africa and the Middle East and took approximately 6–7 days to reach Dunhuang. Samples DN3-DN6 originated from the Taklimakan and Gobi deserts in East Asia. A

---

* Corresponding author.
 E-mail address: huangzhongwei@lzu.edu.cn (Z. Huang).

noticeable contrast was observed in the vertical distribution of the coarse and fine components between the long-range transported (DN1~DN2) and fresh (DN3~DN6) dust plumes. DN1 and DN2 presented comparable dust components (DD = Dc + Df, where Dc and Df are coarse- and fine-mode dust, respectively) and non-dust (ND) component contributions and a high predominance of Dc particles was present with at least 40% of total components in DN3-DN4. The contribution of ND particles was nearly negligible in DN5 and DN6. Lidar observations and model simulation both indicated that the maximum contribution of North African and Middle Eastern dust to the local aerosol loading exceeded 58%. However, the model simulation underestimated the contribution of DN1 by an average of 18% compared to lidar observations because DN1 was not reproduced well. This implies that the vertical distribution of dust should be carefully considered when dust impacts (e.g., radiation effects and air quality) are finely assessed using a model on a regional scale.

1. Introduction

Mineral dust aerosols are widely assumed to be crucial global players in the Earth's system. Mineral dust in the atmosphere can significantly modulate the Earth's radiation budget by scattering and absorbing solar and terrestrial radiation, re-emitting radiation to ultimately affect global temperature (Huang et al., 2014; Twomey, 1991), and getting involved in the formation of clouds and precipitation, thereby altering cloud and precipitation properties (Huang et al., 2006; Li et al., 2011; Seinfeld et al., 2016; Thompson and Eidhammer, 2014). Suspended dust particles can deliver micronutrients to remote ecosystems to enhance their bio-productivity (Hamilton et al., 2022; Mahowald et al., 2005), ultimately affecting the global carbon cycle. Furthermore, airborne dust particles favor the transport of fungal spores and bacteria and negatively impact human health, lifestyle, transportation, and economy (Acosta-Martinez et al., 2015; Gat et al., 2021; Morman and Plumlee, 2013; Schroedter-Homscheidt et al., 2013). All these impacts are closely associated with mineral dust transport.

Dust originating from sources such as the Gobi and Taklimakan Deserts in East Asia, the Saharan Desert, and the Arabian Desert has long been a concern. Many studies have shown that severe dust events in East China, Korea, and Japan mostly originate from East Asian dust sources (Minamoto et al., 2018; Xu et al., 2022). If the dust floating in the atmospheric boundary layer (ABL) over the source area is uplifted to the free troposphere, it can generally be transported over a long range by the westerlies and is often observed over the North Pacific and North America, or even farther away (Huang et al., 2008, 2015; Kawai et al., 2015; Uno et al., 2009). Saharan dust is not only transported northward to Europe and westward to the Caribbean and the West Indies (Barkley et al., 2022; Prospero et al., 2021), but has also been carried eastward to Asia (Ganor and Mamane, 1982; Park et al., 2005; Sugimoto et al., 2019a; Tanaka et al., 2005). Several cases of Middle Eastern and Central Asian dust transport to East Asia have been reported (Lee et al., 2006; Tanaka et al., 2005; Tazaki et al., 2004; Wang et al., 2022). Occasionally, dust from North Africa, Middle East, and Central Asia mix with East Asian dust, leading to complications in separating the influence of multi-source mineral dust (Tanaka et al., 2005). Some studies related to dust deposition in the North Pacific have shown that East Asian dust sources contribute close to half of the total, but only in the proximal offshore regions in the northwestern Pacific (Lee et al., 2006; Tanaka and Chiba, 2006), while dust deposition in the majority of the North Pacific is dominated by non-East Asian sources with an eastward decrease along the westerlies (Hsu et al., 2012). Lee et al. (2010) analyzed 76 dust storm-related events in Hong Kong from 1996 to 2007 to identify and characterize dust sources. They found that 73 dust events (96%) involved non-East Asian sources (Saharan influence was found in 63 events) that were previously not known to impact Hong Kong. These studies show that long-range transport from North Africa, the Middle East, and Central Asia to East Asia is common. Therefore, considering the contribution of non-East Asian dust is necessary to better understand dust impacts in East Asia and the North Pacific.

To date, only a few observational and modeling studies have been conducted to understand remote, non-East Asian dust transport processes and their effects on the climate and environment over East Asia

and the North Pacific. Liu et al. (2022) suggested that a quarter of dust events in East Asia during 2007–2020 originated from the Saharan Desert, which could be transported eastward all year, contributing approximately 35.8% of dust loading in the upper troposphere in Northern China in spring. The Navy Aerosol Analysis Prediction System (NAAPS) and Spectral Radiation Transport Model for Aerosol Species (SPRINTARS) global models suggest that the dust plumes observed in Japan on March 25–27, 2003, and March 7–9, 2005, originated from the Saharan Desert and Arabian Peninsula for approximately 5–10 days, when no significant dust storms existed in the arid regions of China and Mongolia (Park et al., 2005; Tanaka et al., 2005). This suggests that the contributions of dust particles in Japan are mainly from North Africa (50%) and the Middle East (30%), while those from China are just 10% in the dust event on March 25–27, 2003 (Tanaka et al., 2005). More cases captured in the Asian Dust Lidar Network (AD-NET) showed long-range transport of dust from the Saharan Desert through the Middle East and Central Asia to East Asia every year in March or April. These transport pathways often lead over the Caspian Sea, Kazakhstan, and Russia (Sugimoto et al., 2019a). Small dust particles are more likely to be transported over long distances, and the change in particle morphology owing to particle aging is a major cause of the decrease in the depolarization ratio (Pan et al., 2017; Zhou et al., 2021). When the remote-sourced dust plumes arrive in Japan, the extinction coefficient and optical depth of the plume are approximately 0.06 km^{-1} and 0.3, respectively, at their maximum. The particle depolarization ratio and backscattering color ratio of the plume are approximately 0.28 and 0.4, respectively (Sugimoto et al., 2019c). A good example is the lifted dust layer from the Middle East observed over Dushanbe, Tajikistan, on April 12, 2015, which was transported across the Pamir Plateau and Taklimakan Desert and, was also probably found over Nagasaki, Japan, on April 17, 2015 (Hofer et al., 2017; Sugimoto et al., 2019a). Another unusual example is the transport of carbon-bearing dust particles as cloud nuclei from Iraq to Japan during the spring. They were related to the incomplete combustion of oil wells and sandstorms that occurred during the Iraq War (Tazaki et al., 2004). Nevertheless, few studies have focused on the vertical structural characteristics of these dust plumes and the differences in their contributions based on observations and simulations, which are crucial for accurately and finely assessing dust climate and environmental effects.

In this study, the transboundary transport of multi-source dust plumes observed in Dunhuang during a field campaign in the spring of 2012 was investigated to identify sources, vertical structure characteristics, and contributions to local aerosol loading. The remainder of this paper is organized as follows: Section 2 describes the measurement instruments and methodologies; Section 3 describes the detection of multisource dust layers and weather patterns. Section 4 discusses the vertical characteristics of the coarse and fine components and their contributions, and Section 5 presents the summary of the findings.

2. Materials and methods

2.1. Field campaign

A field intensity observation campaign was conducted in Dunhuang

(40.492°N, 94.955°E, 1061 m ASL), based on Lanzhou University's mobile facility, from April 1 to June 16, 2012. The observation station was situated at Xihu Farm, which is located in the Gobi agricultural region at the westernmost fringe of the Hexi Corridor in northwest China. This area is home to approximately 1000 inhabitants and thousands of hectares of farmland. From Fig. 1, the station is surrounded by the Qilian and Altun mountains to the south and the Beishan Mountains to the north; the Kumtag Desert is merely 90 km to the west, and the Taklimakan Desert is farther west; and the Badain Jaran Desert is located east of the Dunhuang Region.

During the field campaign, all measurements were recorded continuously using the container platform, and the observation items included meteorological parameters, column aerosol optical properties, aerosol vertical profile, aerosol scattering and absorption properties, radiation flux, etc. An automatic weather station (WTX520, Vaisala, Finland) and an air sampling inlet were installed at the top of the container, positioned 5 m above ground level. Meteorological parameters (wind speed, wind direction, relative humidity, and air temperature) and PM_{10} concentrations were recorded at a temporal resolution of 1 min. The climate in Dunhuang is characterized by extreme drought conditions, and therefore, the mean air temperature and relative humidity are 18.3 ± 8.1 °C and $21.9 \pm 16.5\%$, respectively. During the observation period, the predominant winds in this region were northeast and southwest, with a maximum hourly averaged wind speed exceeding 10 ms^{-1} (Bi et al., 2017). The PM_{10} concentration was monitored using an ambient particulate monitor (model RP1400a, Rupprecht and Patashnick Corp.) based on the principle of a tapered element oscillating microbalance (TEOM) with a flow rate of 16.7 L min^{-1} (Patashnick and Rupprecht, 1991). The accuracy of PM_{10} concentrations was normally $0.1 \text{ } \mu\text{gm}^{-3}$. Due to the heating of the sampling stream at 50 °C, a partial loss of volatile and semi-volatile aerosol compounds occurred, which resulted in negative PM_{10} concentrations. All these negative values were eliminated from the dataset, which accounted for no more than 1% of the total data. The 10-min averaged data from both instruments were used in this study.

2.2. Ground-based lidar

A polarized micro-pulse lidar (P-MPL, type: MPL-4B) at a wavelength of 527 nm was automatically and continuously operated during this field campaign. The pulse laser energy, pulse repetition rate, and temporal and spatial resolution is 6–8 μJ, 2500 Hz, 1 min, and 30 m, respectively. As reported in our previous studies (Xie et al., 2017; Zhou et al., 2018),

the data products including the aerosol extinction coefficient (EXT), aerosol backscatter coefficient (BKS), backscatter ratio, particle depolarization ratio (PDR), and vertical feature mask, can be retrieved by an automatic detection algorithm based on normalized relative backscattering (NRB) and volume linear depolarization ratio (VLDR). Also, the atmosphere boundary layer heights (ABLH) were determined by the algorithm based on polarized lidar observation (Han et al., 2022). In this study, the optical and mass features of three particle components (coarse dust (Dc), fine dust (Df) and Non-dust (Nd)) were vertically separated using a modified polarized lidar-photometer networking (POLIPHON) algorithm, which is specifically applied to the P-MPL measurements, is based on the specific particle linear depolarization ratio given for different types of aerosols, and can be run in either 1-step (2-component separation) or 2-steps (3-component separation) versions (Córdoba-Jabonero et al., 2018; Mamouri and Ansmann, 2017). A more detailed description of this algorithm is given by (Córdoba-Jabonero et al., 2018). The EXT was obtained by applying Fernald's method (Fernald, 1984) with a lidar ratio of 40 sr for Dc and Df particles and 50 sr for continental aerosols (Nd), which are recommended for Asian dust (Ansmann et al., 2019). The extinction-to-mass conversion procedure was also described, and the relative mass contribution or fraction of each aerosol component (i) was defined as the ratio of $\overline{M_i}$ to TMC, where $\overline{M_i}$ is the height-integrated mass concentration (gm^{-2}) of each component (i), and $\text{TMC} = \sum \overline{M_i}$ represents the total mass loading (gm^{-2}) (Córdoba-Jabonero et al., 2018). The $\overline{M_i}$ was computed by dividing the extinction coefficient of each component by their specific mass extinction efficiency (MEE: k, m^2g^{-1}). The MEEs for Asian dust were separately calculated by adopting the dust particle density of 2.6 g cm^{-3}, and the volume-to-extinction conversion factor of 0.27×10^{-12} Mm for Df and 0.94×10^{-12} Mm for Dc, respectively, which were determined based on the aerosol robotic network (AERONET) long-term dust observations at semi-arid climate and environment observatory of Lanzhou University (SACOL) (Ansmann et al., 2019).

2.3. Other data and tools

To trace the origins of the different dust plumes and assess the respective contributions of dust from different sources to the aerosol loading in Dunhuang, the WRF-Chem was employed, which is updated by the University of Science and Technology of China (named USTC version). The USTC version includes additional capabilities, such as contribution analysis of aerosol-related processes and improved turbulent mixing of aerosols, compared to the publicly released version (Hu
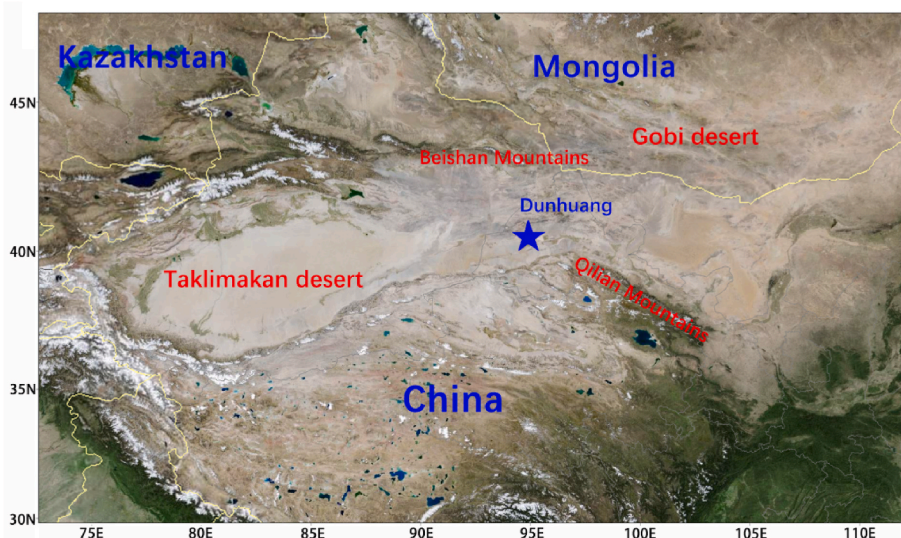

Fig. 1. Location of the field intensity observation campaign in Dunhuang (blue star), northwest China.

et al., 2020; Ruan et al., 2022; Zhao et al., 2013a, 2013b). The Model for Simulating Aerosol Interactions and Chemistry (MOSAIC) (Zaveri et al., 2008) was used in the aerosol scheme with eight aerodynamic diameter ranges between the adjacent diameters (0.039, 0.078, 0.156, 0.3125, 0.625, 1.25, 2.5, 5, and 10 μm) The aerosol components, including mineral dust and anthropogenic emissions, were simulated, and the mineral dust was calculated separately for the four sources that are United States, East Asia, North Africa, and other regions). The Rapid Radiative Transfer Model for General Circulation (RRTMG) (Iacono et al., 2008) was used to calculate long- and short-wave radiations and aerosol radiation feedback. In this study, the initial meteorological fields and lateral boundary conditions were obtained from the National Center for Environmental Prediction final analysis (NCEP/FNL) datasets, which have a 1° horizontal resolution and are provided at 6 h intervals. The simulation was configured with a horizontal resolution of 111 km and 49 vertical layers, up to 100 hPa. The domain covered the region from 15° S to 65° N and 30° W to 160° E, with a grid consisting of 190 × 80 pixels.

Furthermore, the study utilized the Level 1 V4 and Level 2 Vertical Feature Mask products provided by CALIPSO (Cloud-Aerosol Lidar and Infrared Pathfinder Satellite Operation) to support the long-range transported dust plumes (Winker et al., 2010). MOD08_D3 products obtained from the Moderate Resolution Imaging Spectroradiometer

(MODIS) were used to examine the spatiotemporal changes in aerosol optical depth (AOD) over East Asia (Levy et al., 2013). The ERA5 reanalysis dataset was employed to describe the evolution of the geopotential height-wind field at the 500, 700, and 850 hPa levels, and provided the atmosphere boundary layer heights (Olauson, 2018). To determine air mass trajectories, a HYbrid Single-Particle Lagrangian Integrated Trajectory (HYSPLIT) model developed by the National Oceanographic and Atmospheric Administration (NOAA) in collaboration with Australia's Bureau of Meteorology was employed (Stein et al., 2015).

3. Results

3.1. Dust plumes determined by P-MPL

From April 5–10, 2012, the coexistence of multiple notable aerosol plumes were detected by the P-MPL in Dunhuang, as illustrated by the NRB and VLDR in Fig. 2a and b. During April 5–7, the weak plumes can be clearly observed in Fig. 2b. Starting at approximately 18 UTC on April 5, the first evident plume (marked DN1 in Fig. 2b, hereinafter the same abbreviations) commenced at heights around 4–6 km. This plume maintained a thickness of approximately 2 km and persisted for at least 35 h, until approximately 05 UTC on April 7. The top height of DN1
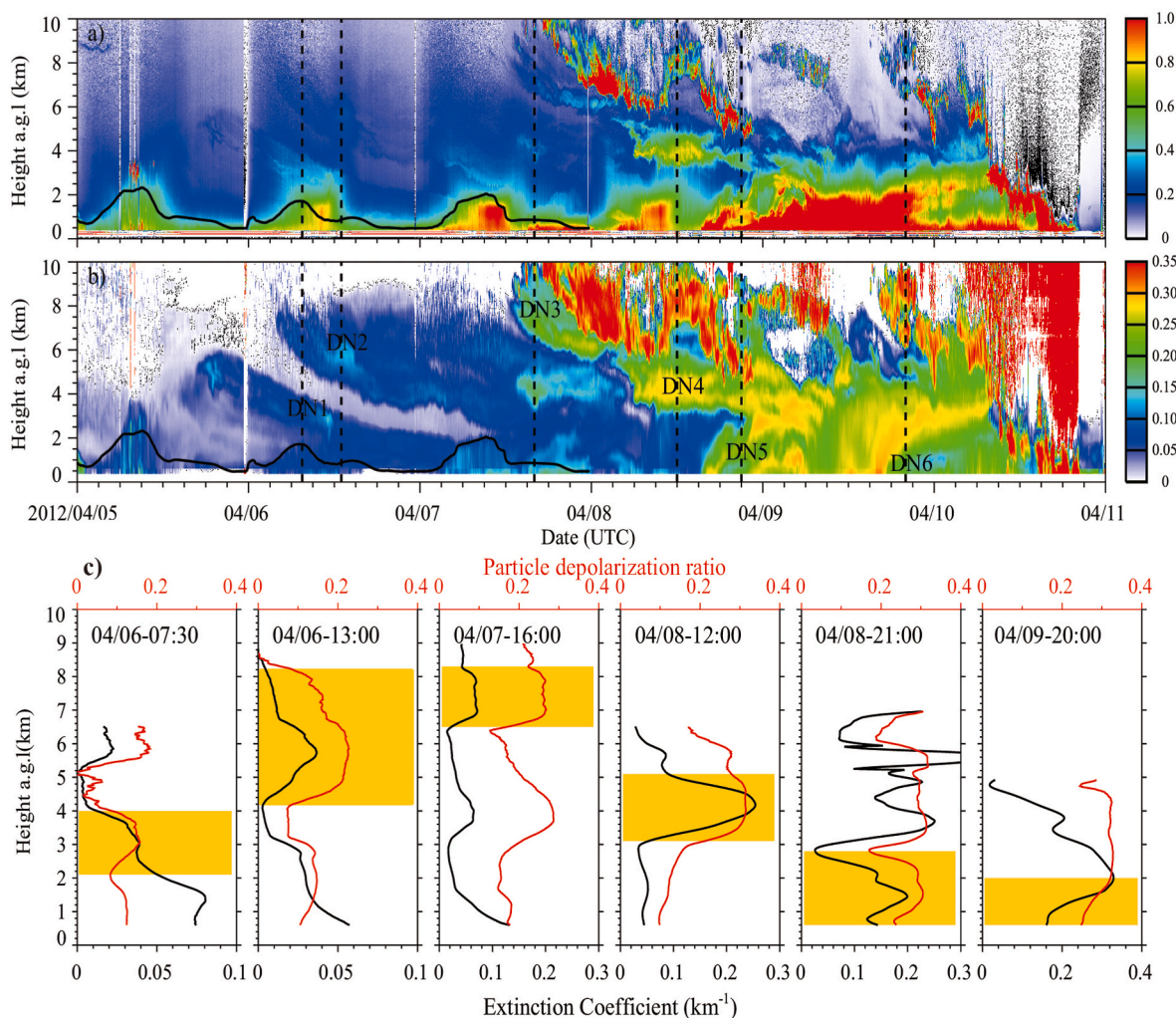

Fig. 2. Time-height cross-section of MPL observations from 5 to April 10, 2012 in Dunhuang at 527 nm wavelength: a) NRB (Normalized Relative Backscattering, counts km² μJ⁻¹μs⁻¹); b) VLDR (Volume Linear Depolarization Ratio); c) profiles of MPL-derived total aerosol extinction coefficient and PDR (Particle Depolarization Ratio) representing DN1~DN6, which are labeled by black dash lines in a) and b). The black solid lines represent atmosphere boundary layer height (ABLH) determined by the algorithm in the previous study (Han et al., 2022). The yellow shadow areas indicate the selected dust layers.

gradually decreased with time. After approximately 12 UTC on April 6, DN1 intruded the ABL. Above DN1, the second plume (DN2) appeared at a height approximately 7 km, starting at approximately 04 UTC on April 6 and persisting for over 36 h. Subsequently, DN2 expanded to a maximum thickness of approximately 5.6 km at approximately 21 UTC on April 6. The bottom height of DN2 remained above 3 km and was consistently at least 1 km higher than that of DN1. DN1 and DN2 were characterized by low VLDRs and long-lasting durations, suggesting their long-range transport from elsewhere. Simultaneously, DN3, with a high VLDR, was observed at altitudes around 5.5–10 km, with a relatively high NRB. Compared to DN1-DN3, DN4 had the highest NRB and VLDR, starting at approximately 06 UTC on April 8, and almost suspended at altitudes of approximately 3–5 km. Starting at approximately 15 UTC on April 8, the aerosol layer near the ground surface passed over the observation station until precipitation at approximately 12 UTC on April 10, which had a thickness of at least 4 km. As shown by the evolution of this aerosol plume height with high VLDRs, which continuously increased from the surface to approximately 3 km from 17 UTC on April 9 to 07 UTC on April 10, another air mass may have passed. Therefore, this aerosol layer was separated into two sub-periods and marked as DN5 and DN6.

As we know, the fresh dust particles over the source or near the source region have a large depolarization ratio. While the microphysical and optical properties of dust particles change during long-distance transport, changes in size due to gravity setting and morphology due to aging generally cause a decrease in the depolarization ratio, with changes in morphology being the major cause (Pan et al., 2017; Sugimoto et al., 2019b). Therefore, to some extent, the depolarization ratio can reflect the degree of dust particles aging. Dust particles transported over long distances tend to remain in the atmosphere for longer periods, leading to a more significant aging process. Thus, these particles exhibit a lower depolarization ratio than those of freshly emitted dust particles. Here, the six profiles of the EXT and PDR marked in Fig. 2b were selected to represent the DN1-DN6 plumes. Based on previous studies (Chen et al., 2007; Córdoba-Jabonero et al., 2018; Mamouri and Ansmann, 2014, 2017), a PDR of 0.05 was widely employed as an indicator to distinguish the dust-like particles (high PDR) from non-dust (ND) particles (low PDR). It can be seen in Fig. 2c that the PDR of all plumes is exceed 0.05. Obviously, DN3-DN6 have high PDR, which indicate these plumes in Fig. 2b are dust plumes. To further confirm that DN1 and DN2 are dust plumes, the CALIOP observations have been shown in Fig. 3,

which are just observed at approximately 19:23 UTC on April 5 and at approximately 20:06 UTC on April 6. It can be found that aerosol subtype in Vertical Feature Mask product indicate that mineral dust and polluted dust exist near Dunhuang.

As summarized in Table 1, the mean PDRs of DN3-DN6 are approximately 1.4–2.3 times higher than those of DN1-DN2. The means PDRs of DN3-DN6 are at least 0.25, which are close to the fresher characteristics of pure dust particles (Liao et al., 2023), and the PDRs of DN1 and DN2 show the intermediate values, indicating they are the mixture of dust particle. Additionally, the mean EXT in DN1-DN2 range from 0.018 km^{-1} to 0.035 km^{-1}, which were of the same order as the values of long-range transported non-East Asian dust cases reported by Park (Park et al., 2005) and Sugimoto (Sugimoto et al., 2019a,b,c). The EXT of DN4-DN6 was 2–16 times higher than that of DN1-DN3, but they were approximately 16–33% of the 0.87 km^{-1} dust plumes which completely attenuated the laser beam observed at 20 UTC on April 22 during the same campaign (Zhou et al., 2018). Thus, the dust plumes determined in this study were characterized by low and medium concentrations.

3.2. Synoptic situations and regional aerosol evolution

Fig. 4 show the time series of meteorological parameters near the ground surface in Dunhuang station during April 5–10, 2012. It can be seen that the wind direction appears to be scattered, and the wind speeds almost remain below 6 ms^{-1} until approximately 17 UTC on April 9. During this period, there was a noticeable decrease in air pressure, and relative humidity, while air temperature increased. Meanwhile, the relative humidity and air temperature exhibited a weakening of the diurnal variation. After approximately 17 UTC on April 9, an increase in both air pressure and relative humidity was observed. The air temperature dropped from 19.2 °C to −1.2 °C during from approximately 15 UTC on April 9 to 00 UTC on April 11. During this period, a sharp change in wind direction, transitioning from southwest to northeast, was

Table 1
The summary of mean values in six vertical profiles for DN1-DN6.

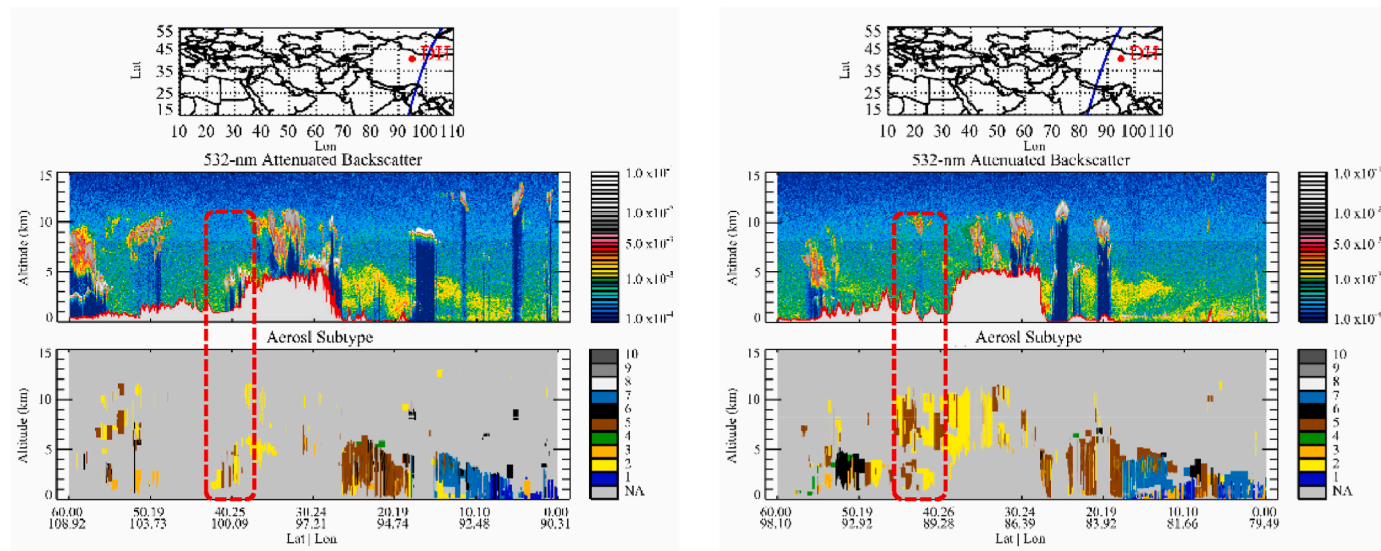|	DN1	DN2	DN3	DN4	DN5	DN6
EXT (km^{-1})	0.035	0.018	0.06	0.18	0.14	0.29
PDR	0.13	0.18	0.25	0.30	0.27	0.28

Fig. 3. CALIOP overpassing orbits and lidar transect. Left panels: at 19:23 UTC on April 5, 2012; Right panels: at 20:06 UTC on April 6, 2012. The red boxes indicate the area near Dunhuang. In the bottom panel: the colored bar-code denotes: N/A = not applicable, 1 = marine, 2 = dust, 3 = polluted continental/smoke, 4 = clean continental, 5 = polluted dust, 6 = elevated smoke, 7 = dusty marine, 8 = PSC (Polar Stratospheric Clouds), 9 = volcanic ash, 10 = sulfate/other.
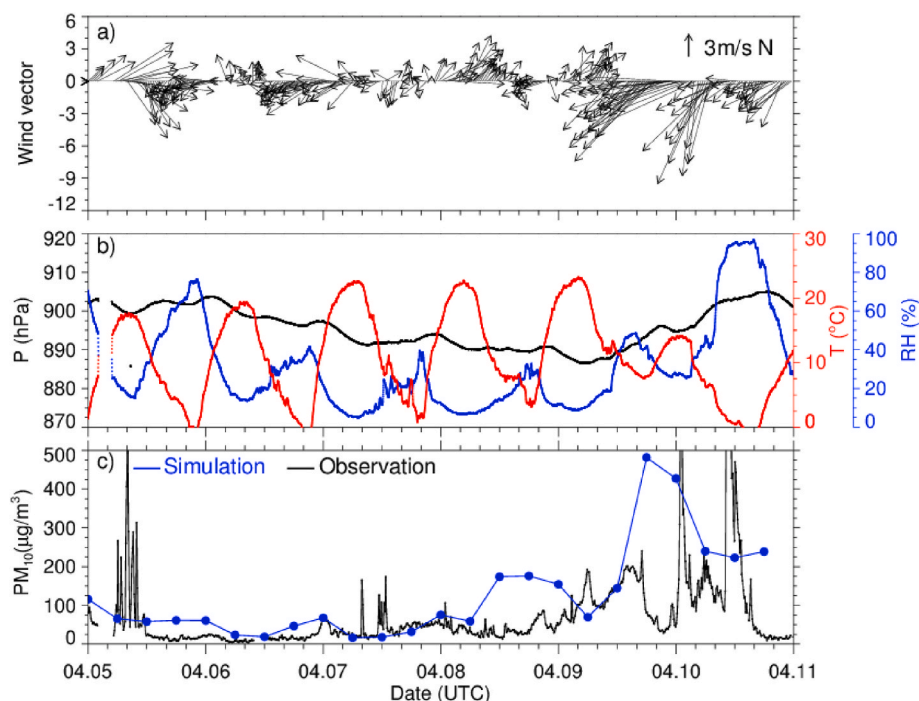
Fig. 4. Meteorological parameters near the ground surface from 5 to April 11, 2012 in Dunhuang: a) wind speed and direction; b) air pressure, relative humidity, and air temperature at 5 m height a.g.l. ; c) PM10 concentration by in situ observation (black line) and the lowest layer (382 m a.g.l) of model simulation (blue line).

observed, and the wind speeds strengthened from approximately 6 ms^{-1} to more than 10 ms^{-1}. These features indicate that the cold front passes over Dunhuang, where dust particles are lifted along the surface of the cold front from the dust layer by ascending warm air (Kawai et al., 2015). Evidently, from Fig. 2b, the height of the dust plume was continuously increasing from 17 UTC on April 9 to 07 UTC on April 10. PM_{10} concentration near the ground surface gradually increased and then sharply decreased before approximately 00 UTC on April 10. The mean PM_{10} concentration was $27 \pm 15 \, \mu g \, m^{-3}$ before around 17 UTC on April 9. Subsequently, the mean PM_{10} concentration reached 102 ± 55 $\mu g \, m^{-3}$ with a maximum of $241 \, \mu g \, m^{-3}$ at approximately 17 UTC. The PM_{10} concentrations during the study period were lower than the average level of $113 \pm 169 \, \mu g \, m^{-3}$ over the entire field campaign (Bi et al., 2017).

Fig. 5 shows the circulation pattern at the 500, 700, and 850 hPa levels on a larger spatial scale during the period of April 2–9. On April 2–4, strong winds can be found over North Africa and the Arabian Peninsula at 850 hPa level, which is a favorable condition for large-scale sand driving and sand dust transport upward. Meanwhile, on April 2–4, the Southwestern Europe region was continuously controlled by a strong low-pressure system, and the center of the low-pressure weakened as it moved eastward. As a result, On April 2–3, a strong southwesterly wind prevailed over North Africa and Arabian Peninsula region at 700 hPa and 850 hPa levels and continued to move northeast, which drove the uplifted dust transport from North Africa and the Arabian Peninsula to East Asia. Over the north of Northwest China, the wind changed from southwesterly wind to westerly or northwesterly wind, which caused the air mass containing dust particles to intrude the northwest of China. Also, it can be seen that a strong easterly wind prevailed over Tarim Basin (TB) at 850 hPa on April 5. Subsequently, the prevailing winds gradually changed to the northeast and southeast on April 6–7, which were associated with the airflow movement of anticyclones in the TB, and this is the one of key reasons that the dust storms frequently occur in springtime in the TB region (Zhou et al., 2023). On April 8–9, with the strengthening and eastward movement of the anticyclones at 700 and 850 hPa levels over Kazakhstan, northerly winds prevailed near the surface around Dunhuang and the wind speed increased.

The spatiotemporal evolution of the daily AOD over Asia from April 5–10, 2012 is shown in Fig. 6. The high AOD area exhibited an evolutionary trend in the clockwise direction in the order of the southwest, west, northwest, north, and northeast sides of the TB from April 5–9. This evolution is always associated with the airflow movement of anticyclones in the TB, and the dust storms often occur (Yumimoto et al., 2019). However, the AOD gradually decreased with time from April 5–9 and traveled eastward to Dunhuang. On April 10, another high-AOD area was found in western Mongolia and western Inner Mongolia, indicating that another dust event occurred in the Gobi Desert. These types of dust events are related to the southward movement of strong cold air and affect the dust load in the TB. The weather forms corresponding to the two major dust events in northwest China before and after April 9 can also be seen in Figs. 4 and 5.

3.3. Source identification

The dust layers marked in the profiles of Fig. 2c were investigated to trace the sources of DN1-DN6. As shown in Fig. 7a, the backward trajectory of DN1 clearly show that air mass traveled through West Asia and Central Asia in approximately 4–5 days. The altitude of the trajectory is below 2 km over Uzbekistan and Kazakhstan, which mixes easily with the atmosphere boundary layer and carries local dust particles over long distances. Also, the low PDRs in DN1 indicated dust particles that have undergone significant aging owing to long-range transport. Similar to DN1, the backward trajectories of DN2 provided clear evidence of its origin in North Africa and Arabian Peninsula in Fig. 7b. These two air masses were transported to the northeast and merged into a single dust cluster over Central Asia in approximately 6–7 days. Furthermore, the transport path observed in this case was similar to those reported in previous studies on African and Middle Eastern dust events (Park et al., 2005; Tanaka et al., 2005). As mentioned in Section 3.1, the subsequent dust plumes (DN3-DN6) with high PDRs were relatively easy to determine. As shown in the AOD map in Fig. 6, the dust behavior was consistent with the airflow anticyclone in the TB on April 5–8. This type of dust behavior is common in TB, where the dust particles are often uplifted (7–9 km) to the free troposphere over the TB (Meng et al., 2019;
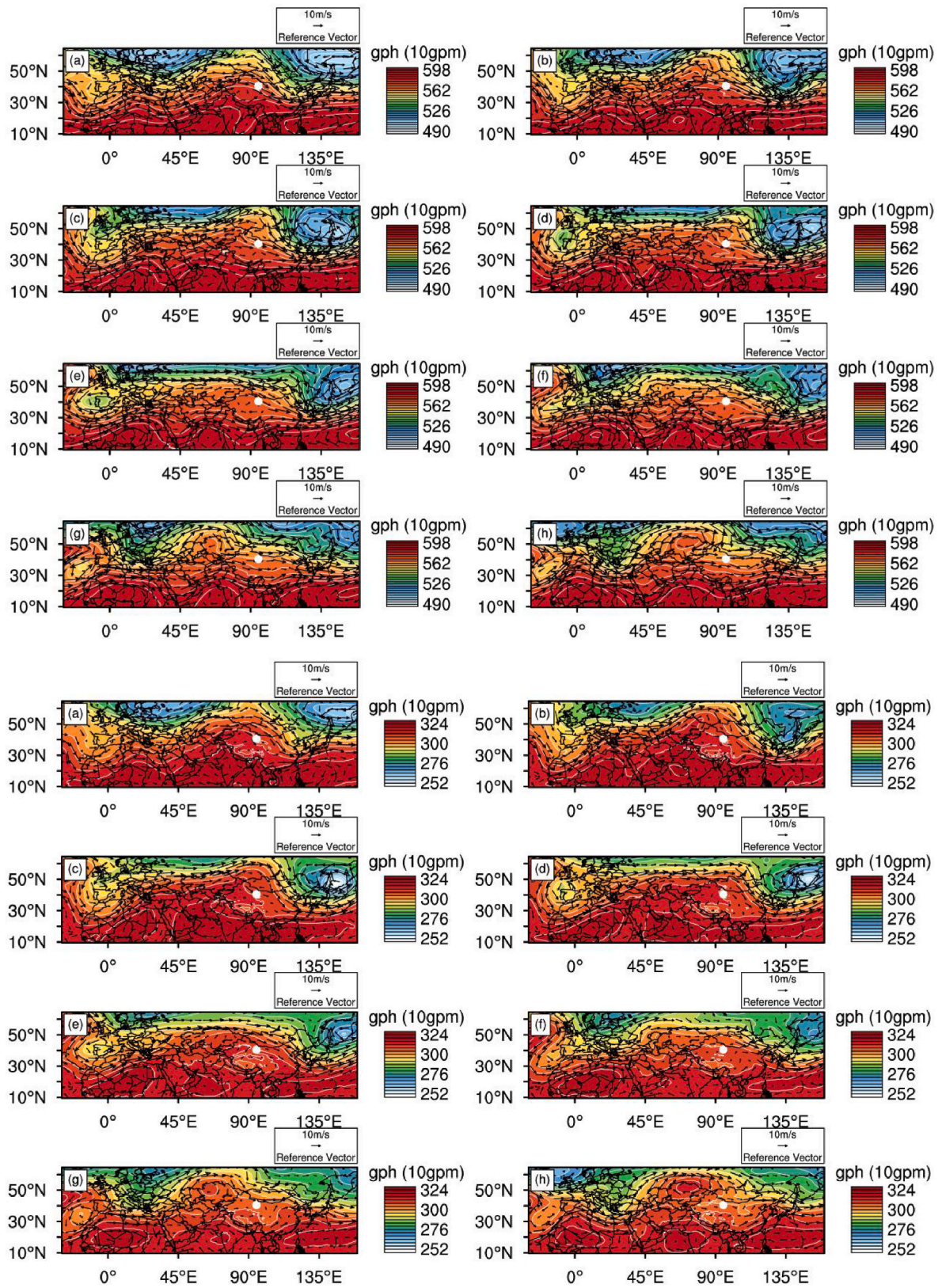
Fig. 5. The geopotential height (color shade) and wind field at 500 hPa level on (a) 2; (b) 3; (c) 4; (d) 5; (e) 6; (f) 7; (g) 8; (h) April 9, 2012 using ERA5 reanalysis dataset. The white dot indicates the location of Dunhuang.
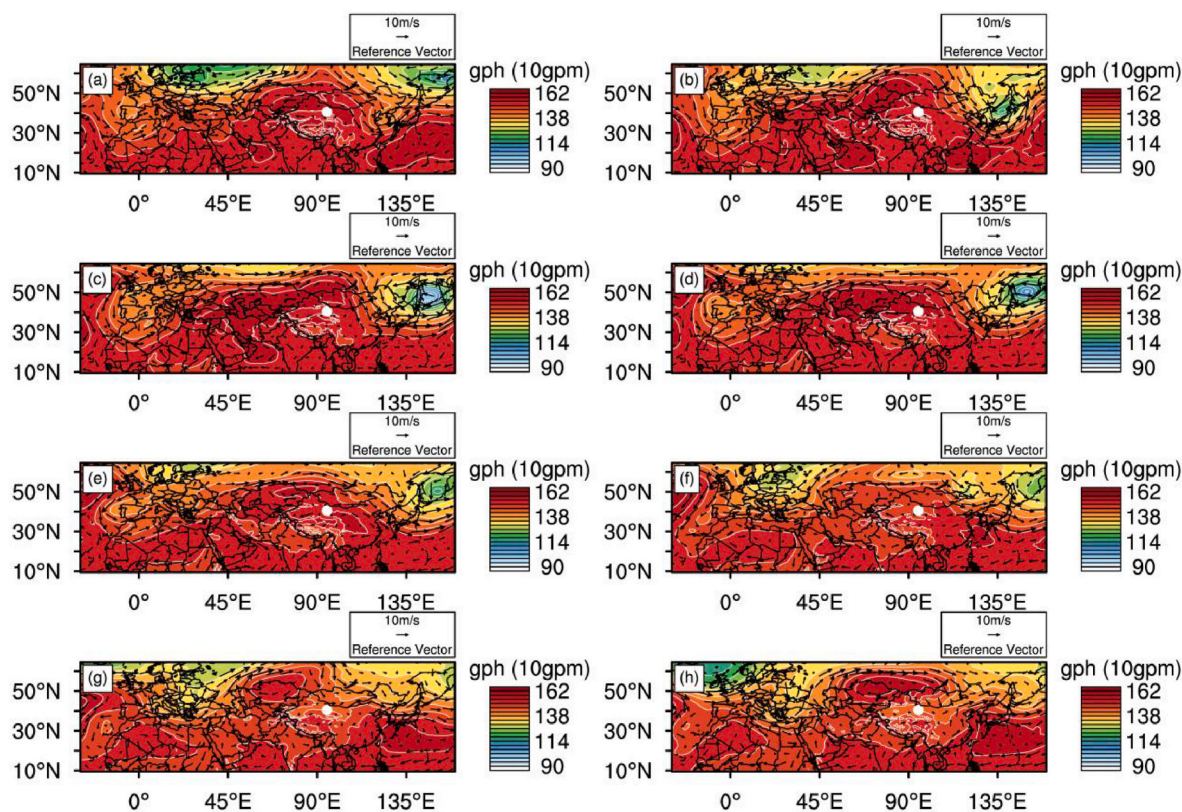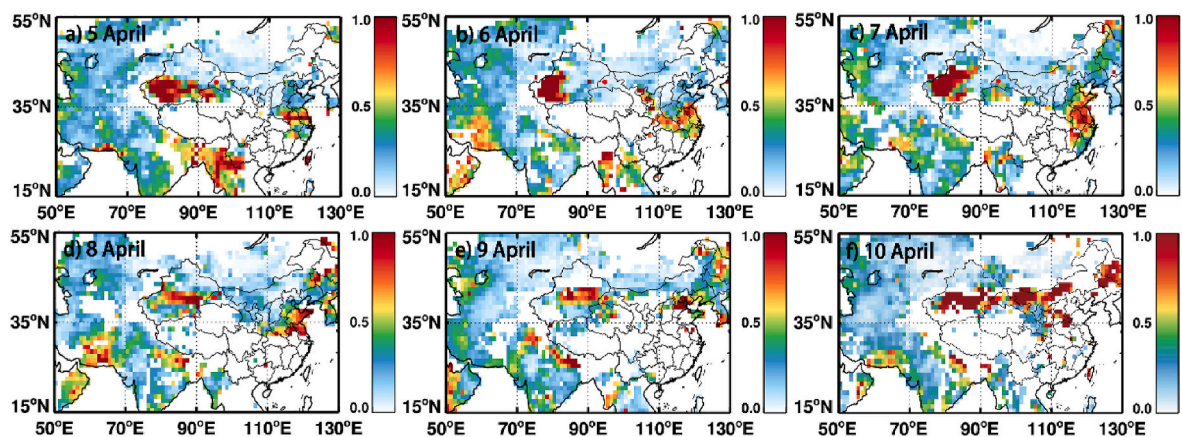
Fig. 5. (*continued*).

Fig. 6. Daily spatio-temporal distribution of aerosol optical depth (AOD) derived from MODIS over the Asian region during 5~April 10, 2012.

Zhou et al., 2013). Moreover, suspended dust layers at a height of 3–5 km remain for a long time over the TB (Huang et al., 2009; Zhou et al., 2022). The backward trajectory at 16 UTC on April 7 does not clearly show the source of DN3 in Fig. 7c, but the separated simulation of WRF-Chem model suggests that DN3 originate from East Asian source. Considering the dust behavior in the TB on April 5–6 in Fig. 6, the evolution pattern of this dust storm is similar with that of case reported by Meng (Meng et al., 2019). In their study, the dust plume in TB could be uplifted to more than 7 km during dust storm. As pointed out by Iwasaka (Iwasaka et al., 2003), these uplifted dust particles from TB can be transported to Dunhuang by the westerly winds. Combining these factors, DN3 could have originated from Taklimakan Desert. The backward trajectory of DN4 were consistent with the wind field in the TB, suggesting that DN4 was also from the Taklimakan Desert. Furthermore,

the backward trajectories for DN5 and DN6 on April 9 suggested that dust was transported from the western observation station within the ABL. However, the air mass trajectories of DN5 originated from the Taklimakan Desert, while that of DN6 pointed towards the Gobi Desert.

4. Discussions

4.1. Vertical characteristics of coarse and fine components

Fig. 8 shows the extinction coefficient of both coarse (α_{Dc}) and fine (α_{Df}) total dust ($\alpha_{DD} = \alpha_{Dc} + \alpha_{Df}$) and non-dust ($\alpha_{ND}$) components for DN1-DN6. Overall, the mixing of Dc, Df, and ND particles was observed below an altitude of approximately 2 km, with the Dc component contributing more significantly than the Df component. This indicates
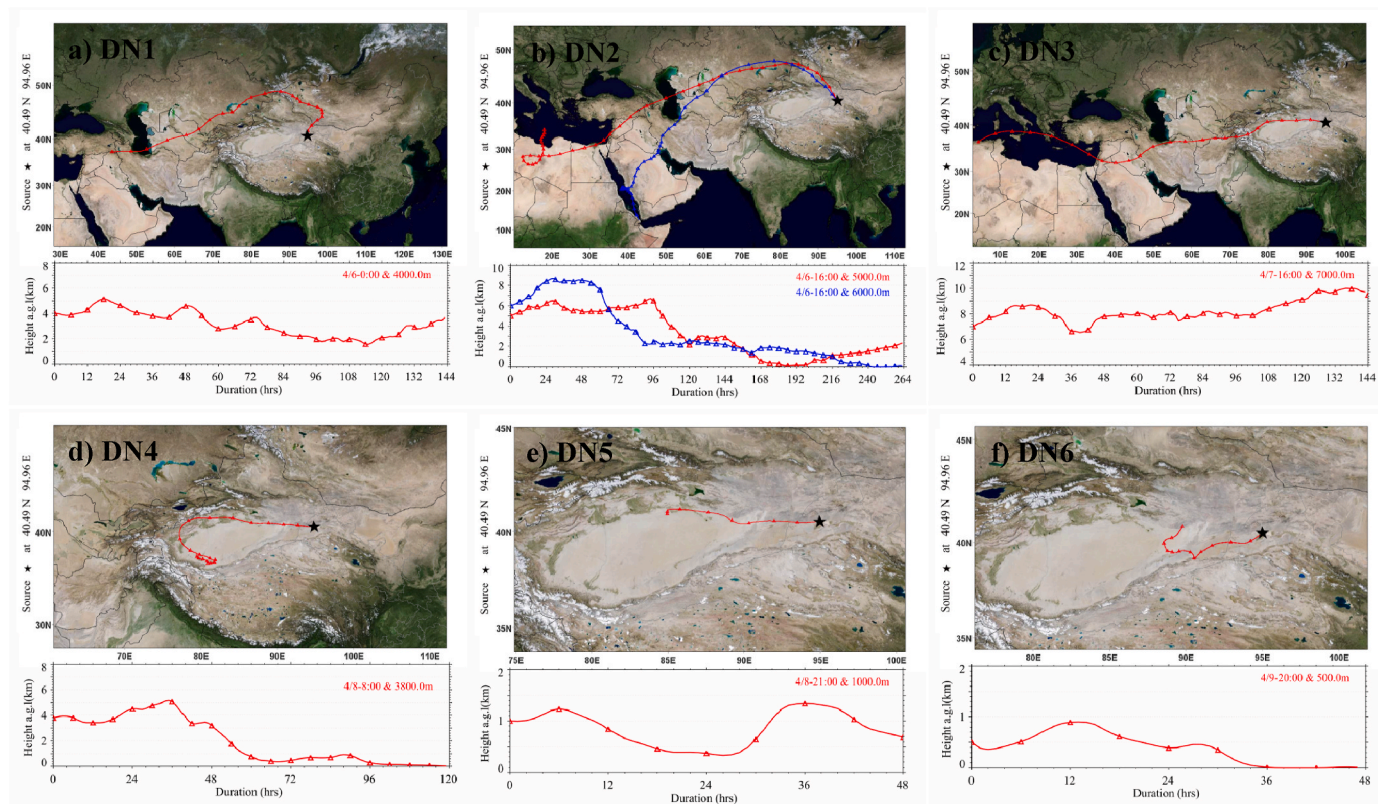
Fig. 7. The air mass backward trajectories started at the corresponding height and time DN1-DN6 in Fig. 2a–b.
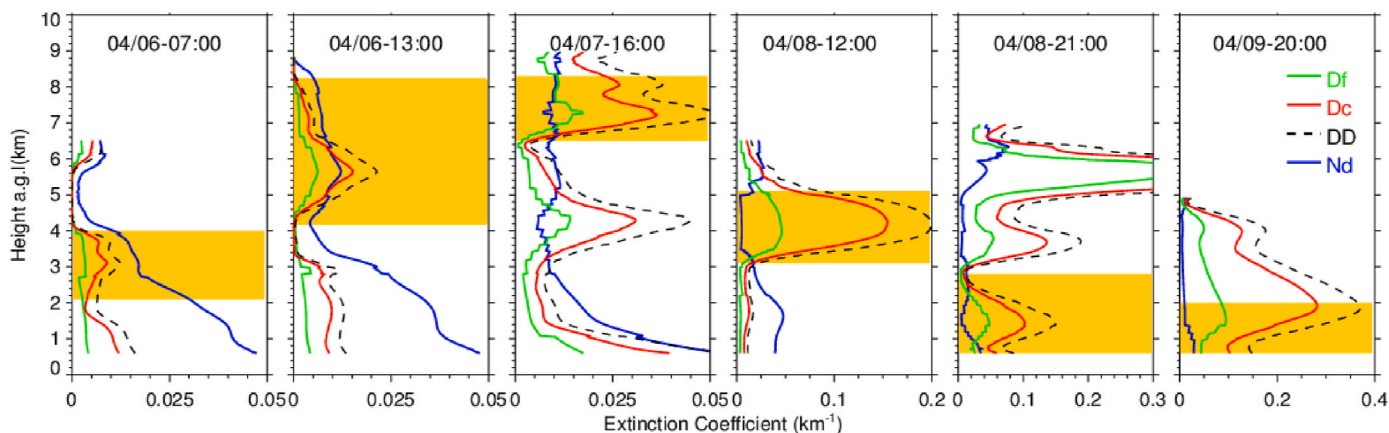

Fig. 8. Vertical profiles of the extinction coefficient of dust-coarse (Dc), dust-fine (Df), dust-total (DD = Dc + Df), and non-dust (Nd) component as derived from the POLIPHON algorithm for the cases in Fig. 2c.

that dust particles were also present below this height during the entire study period (Córdoba-Jabonero et al., 2021). At altitudes below 2 km, the ND particles were dominant and α_{ND} remained relatively unchanged on April 6, and a noticeable increase was observed in Dc and Df particles on April 7. In the case of DN1, the Dc and Df components with the DD peak of 0.012 km^{-1} were primarily observed in the upper part of the atmosphere, while the lower part was dominated by ND particles with a maximum of 0.03 km^{-1}. DN2 exhibited the opposite DD pattern, with the DD layer extending from approximately 4 to 8 km in height and a weak incidence (α_{DD} = 0.021 km^{-1}) observed at approximately 5.6 km. ND particles mostly dominated from 6.8 to 8.6 km. The DD peaks of DN1 and DN2 were approximately 3.2% and 5.7%, respectively, of those given by DN6. The vertical distribution of the Dc, Df, and ND components in DN1 and DN2 confirmed that the dusty air masses mixed with

the non-dusty air masses along the pathway to Dunhuang. Additionally, this distribution easily disturbed the source identification of the dust plumes because they were sensitive to the start time and height of the back trajectories, as described in Section 3.3. On April 7–8, an intensified dust event characterized by a high quantity of Dc components and a two-peak structure in the emerging dust layers was observed at approximately 13 UTC on April 7. In particular, a high predominance of Dc was observed in DN3 and DN4, where α_{DD} peak values were 0.053 km^{-1} and 0.2 km^{-1}, respectively. They showed a lower median dust incidence (14%–54%) compared to that of DN6. The Df and ND components presented similar levels in DN3, and almost no ND signature was detected in DN4. As shown in Fig. 2, a greater incidence of dust intrusion near the ground was observed after 15 UTC on April 8. A pronounced dust layer (DD = Dc + Df, with Dc predominance)

extending from the ground to heights of 4–5 km was observed in DN5 and DN6, respectively; for both, α_{DD} peaks of 0.15 km^{-1} at 1.4 km and 0.37 km^{-1} at 1.9 km were found. Both cases exhibited a high predominance of Dc particles with very small or almost zero ND contributions at the dust layer. These scenarios are similar to those of the Saharan dust cases with a high dust incidence, as reported in previous studies (Córdoba-Jabonero et al., 2018, 2019, 2021). Moreover, DN6 was characterized by a nearly two-thirds decrease in Dc and Df particles near the ground, which is associated with the change in sources of air mass, as stated in the above sections.

Fig. 9 shows the temporal evolution of the relative mass contribution of each aerosol component throughout the study period. Overall, the relative contribution of Df particles was not greater than 11%. Two different scenarios with weak and intense dust impacts were observed before and after approximately 13 UTC on April 7. A high loading of Dc particles with a peak of 91.3% was obtained at approximately 00 UTC on April 8, and the Dc particles remained at a high loading level (72.1%–91.3%) from 13 UTC on April 7 to 04 UTC on April 10. Before this time, a gradual Dc loading increased from approximately 19.3% to these high values. Here, the TMC increased from 0.02 g m^{-2} to 0.76 g m^{-2}. The mean TMC values of 0.16 ± 0.14 g m^{-2} and 3.28 ± 2.40 g m^{-2} were estimated for weak and intense dust impact periods, respectively. In this study, the mean mass concentration of DD fraction at TMC for the intense dust impact period (3.28 ± 2.40 g m^{-2}) was 4 times higher than 0.7 ± 0.4 g m^{-2} found at Barcelona and 16–23 times higher than 0.14 ± 0.03 and 0.20 ± 0.04 g m^{-2} observed at Leipzig (Córdoba-Jabonero et al., 2021).

4.2. Contribution of non-East Asian dust

To assess the effects of non-East Asian dust to local aerosol loading in Dunhuang, the contributions in column and vertical distribution were obtained by using WRF-Chem simulation and lidar observations. Here, the comparison of mass concentration near the ground surface from WRF-Chem simulation and in-situ observation was given in Fig. 4c, which indicated that the WRF-Chem model was in good agreement with observations during the period from April 5 to April 8. As shown in Fig. 10, the East Asian dust remained dominant during most of the study period. The total dust column concentration maintained within 100 mg/m^2 over Dunhuang before April 8 (Fig. 10a). North African dust exhibited a gradual increase in column mass concentration since April 6, reaching its peak at approximately 1200 UTC on April 7. The Middle Eastern dust also showed a variation and amplitude similar to those of the North African dust. The combined contribution of North African and Middle Eastern dust to local dust column concentration ranged of 55%–83% from 06 UTC on April 6 to 18 UTC on April 7. Simultaneously, their

total contribution to dust concentrations near ground surface in Dunhuang reached a peak of approximately 39% at 12 UTC on April 7 in Fig. 10b.

Fortunately, dust plumes such as DN1 and DN2, which remained relatively independent from other East Asian dust layers (e.g., DN3-DN6) before intruding the ABL, provided an excellent opportunity to assess their contribution based on the perspective of aerosol extinction coefficient retrieved from lidar. The spatiotemporal evolution in Fig. 2 shows that a significant portion of DN1 and DN2 was situated above the ABL. As shown in Fig. 2a and b, it can be seen that when the height of DN1 and DN2 descended below the maximum ABLH on April 5–7, they were likely to mix with aerosols in the residual boundary layer, and lidar cannot distinguish between them. Therefore, the maximum ABLH of 2 km on April 5–7 was set to extract DN1 and DN2 from the boundary layer aerosol from 12 UTC on April 5 to 06 UTC on April 7. Thus, the AOD above 2 km was assumed to represent the sum of AOD for DN1 and DN2. The ratios of the AOD above 2 km to the total AOD were calculated to represent the contributions of DN1 and DN2. The same calculation was also applied for the contribution using the WRF-Chem model but for mass concentration. As shown in Fig. 11, the period between 18 UTC on April 5 and 06 UTC on April 7 should be focused on due to the DN1 just passing over the observation station and DN2 just being mixed with aerosol in ABL. The maximum contribution reached approximately 58% for lidar observation at 12 UTC and 74% for model simulation at 18 UTC on April 6, respectively. Overall, model simulation overestimated the cumulative contribution by nearly 9%. Before 06 UTC on April 6, the contribution using the model was an average of 18 % lower than that by lidar assessment. This underestimation can be mainly associated with that the model with a coarse spatial resolution did not reproduce DN1 detected by lidar over Dunhuang. In addition, the differences in the height and concentration of DN2 simulated by the model can be used to explain the overestimation after 06 UTC on April 6. Usually, the validation and constraints for model simulation are conducted by using the surface mass concentration or AOD, while the results in this study imply that the vertical distribution of dust layers should also be carefully considered when accurately assessing the dust radiation effects at the regional scale.

5. Conclusions

Transboundary transport of multi-source mineral dust was captured during April 5–10, 2012, using the P-MPL system during an intensive field campaign in Dunhuang, northwest China. In this study, six dust plumes (DN1-DN6) determined by the spatiotemporal evolution of the VLDRs were selected. Subsequently, the source characteristics, coarse and fine components, and their relative contributions were investigated.
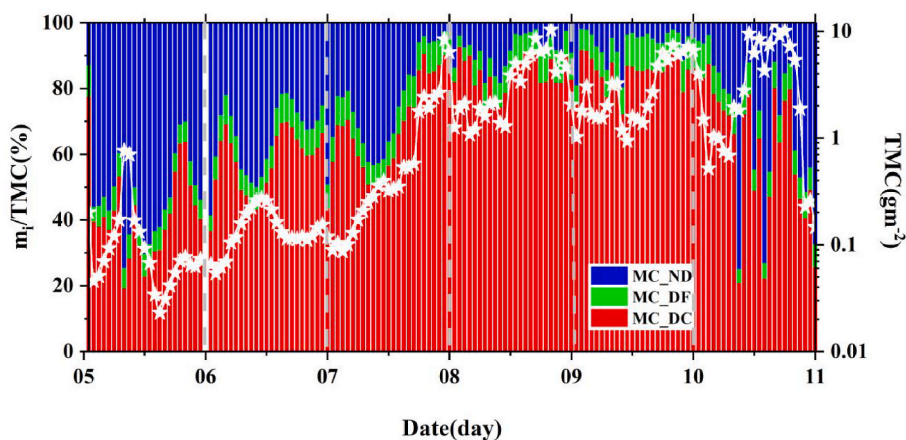

Fig. 9. (Left axis) The POLIPHON-derived relative contribution of mass loading for Dc (red), Df (green), and Nd (blue) components to concerning the column total mass concentration (TMC, g m^{-2}) with is also shown by white stars (Right axis).
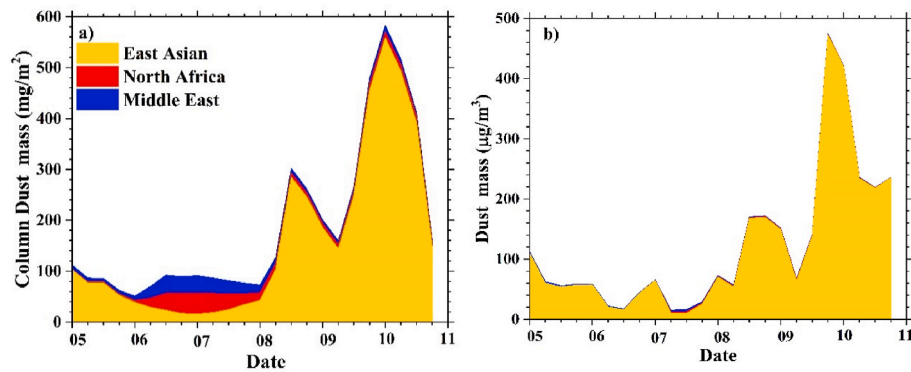
Fig. 10. The dust mass concentration of different dust sources over Dunhuang. a) the column mass concentration; b) the mass concentration at the lowest level of the model (382 m a.g.l).
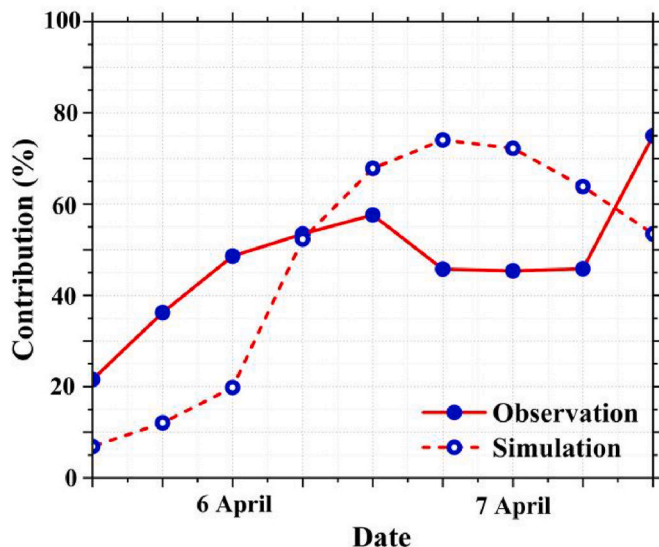

Fig. 11. The contribution of African dust and Middle East dust above 2 km to the total column aerosol loading based on lidar observation and WRF-Chem simulation in Dunhuang, respectively.

The results showed that DN1 and DN2 were transported over long distances to the observation station, and the DN1 was from Central Asia and it took approximately 4–5 days. DN2 was transported from long distances of North African and Middle Eastern dust, which took approximately 6–7 days. Sample DN3~DN6 originated from the Taklimakan and Gobi Deserts in East Asia. A significant difference in the vertical structure of the coarse and fine components existed between the long-range transported dust and fresh dust plumes. For example, the weak α_{DD} peak of DN1 and DN2 was less than 0.021 km^{-1} and presented comparable levels of DD and ND contributions. The predominance of Dc particles was high with at least 40% of total components in DN3-DN4 and α_{DD} peaked between 0.053 km^{-1} and 0.2 km^{-1}. The α_{DD} peaks of DN5 and DN6 were 0.15 km^{-1} and 0.37 km^{-1} and almost zero contribution of ND aerosols was observed. The model simulation showed that the contribution of North African and Middle Eastern dust to the local aerosol dust column concentration was a range of 55%–83% from 06 UTC on April 6 to 18 UTC on April 7, and to dust concentrations, near-surface reached a peak of approximately 39% at 12 UTC on April 7. The maximum contribution to total aerosol loading assessed by lidar observation and model simulation reached approximately 58% and 74%, respectively. The contribution given by the model simulation was on average 18% lower than that of lidar observations because the model did not reproduce DN1 well. This implies that the vertical distribution of the dust layer should be carefully considered when dust impacts (e.g., radiation effects and air quality) are finely assessed using the model on a regional scale. Long-range transport cases of North African and Middle Eastern dust have often been observed over northwest China, but our understanding of their characteristics and effects over East Asia is still insufficient. In the future, more efforts should be made to combine model simulations and ground-based lidar network observations.

CRediT authorship contribution statement

Tian Zhou: Formal analysis, Investigation, Methodology, Conceptualization, Writing – review & editing. **Xiaowen Zhou:** Investigation, Visualization, Writing – original draft. **Zining Yang:** Software. **Carmen Córdoba-Jabonero:** Software. **Yufei Wang:** Investigation, Visualization. **Zhongwei Huang:** Funding acquisition, Resources, Data curation. **Pengbo Da:** Visualization. **Qiju Luo:** Visualization. **Zhijuan Zhang:** Visualization. **Jinsen Shi:** Data curation. **Jianrong Bi:** Data curation. **Hocine Alikhodja:** English Revision.

Declaration of competing interest

The authors declare that they have no known competing financial interests or personal relationships that could have appeared to influence the work reported in this paper.

Data availability

The authors do not have permission to share data.

Acknowledgments

References

Acosta-Martinez, V., Van Pelt, S., Moore-Kucera, J., Baddock, M.C., Zobeck, T.M., 2015. Microbiology of wind-eroded sediments: current knowledge and future research directions. Aeolian Res. 18, 99–113.

Ansmann, A., Mamouri, R.E., Hofer, J., Baars, H., Althausen, D., Abdullaev, S.F., 2019. Dust mass, cloud condensation nuclei, and ice-nucleating particle profiling with polarization lidar: updated POLIPHON conversion factors from global AERONET analysis. Atmos. Meas. Tech. 12, 4849–4865.

Barkley, A.E., Pourmand, A., Longman, J., Sharifi, A., Prospero, J.M., Panechou, K., Bakker, N., Drake, N., Guinoiseau, D., Gaston, C.J., 2022. Interannual variability in the source location of North African dust transported to the amazon. Geophys. Res. Lett. 49.

Bi, J., Huang, J., Shi, J., Hu, Z., Zhou, T., Zhang, G., Huang, Z., Wang, X., Jin, H., 2017. Measurement of scattering and absorption properties of dust aerosol in a Gobi farmland region of northwestern China - a potential anthropogenic influence. Atmos. Chem. Phys. 17, 7775–7792.

Córdoba-Jabonero, C., Sicard, M., Ansmann, A., del Aguila, A., Baars, H., 2018. Separation of the optical and mass features of particle components in different aerosol mixtures by using POLIPHON retrievals in synergy with continuous polarized Micro-Pulse Lidar (P-MPL) measurements. Atmos. Meas. Tech. 11, 4775–4795.

Córdoba-Jabonero, C., Sicard, M., del Aguila, A., Jimenez, M., Zorzano, M.-P., 2019. Performance of a dust model to predict the vertical mass concentration of an extreme Saharan dust event in the Iberian Peninsula: comparison with continuous, elastic, polarization-sensitive lidars. Atmos. Environ. 214.

Córdoba-Jabonero, C., Sicard, M., Lopez-Cayuela, M.-A., Ansmann, A., Comeron, A., Zorzano, M.-P., Rodriguez-Gomez, A., Munoz-Porcar, C., 2021. Aerosol radiative impact during the summer 2019 heatwave produced partly by an inter-continental Saharan dust outbreak - Part 1: short-wave dust direct radiative effect. Atmos. Chem. Phys. 21, 6455–6479.

Chen, W.-N., Tsai, F.-J., Chou, C.C.K., Chang, S.-Y., Chen, Y.-W., Chen, J.-P., 2007. Optical properties of Asian dusts in the free atmosphere measured by Raman lidar at Taipei, Taiwan. Atmos. Environ. 41, 7698–7714.

Fernald, F.G., 1984. Analysis of atmospheric lidar observations - some comments. Appl. Opt. 23, 652–653.

Ganor, E., Mamane, Y., 1982. Transport of saharan dust across the eastern mediterranean. Atmos. Environ. 16, 581–587.

Gat, D., Reicher, N., Schechter, S., Alayof, M., Tarn, M.D., Wyld, B.V., Zimmermann, R., Rudich, Y., 2021. Size-resolved community structure of bacteria and fungi transported by dust in the Middle East. Front. Microbiol. 12.

Hamilton, D.S., Perron, M.M.G., Bond, T.C., Bowie, A.R., Buchholz, R.R., Guieu, C., Ito, A., Maenhaut, W., Myriokefalitakis, S., Olgun, N., Rathod, S.D., Schepanski, K., Tagliabue, A., Wagner, R., Mahowald, N.M., 2022. Earth, wind, fire, and pollution: aerosol nutrient sources and impacts on ocean biogeochemistry. Ann. Rev. Mar. Sci 14, 303–330.

Han, B., Zhou, T., Zhou, X., Fang, S., Huang, J., He, Q., Huang, Z., Wang, M., 2022. A new algorithm of atmospheric boundary layer height determined from polarization lidar. Rem. Sens. 14, 5436.

Hofer, J., Althausen, D., Abdullaev, S.F., Makhmudov, A.N., Nazarov, B.I., Schettler, G., Engelmann, R., Baars, H., Fomba, K.W., Mueller, K., Heinold, B., Kandler, K., Ansmann, A., 2017. Long-term profiling of mineral dust and pollution aerosol with multiwavelength polarization Raman lidar at the Central Asian site of Dushanbe, Tajikistan: case studies. Atmos. Chem. Phys. 17, 14559–14577.

Hsu, S.-C., Huh, C.-A., Lin, C.-Y., Chen, W.-N., Mahowald, N.M., Liu, S.-C., Chou, C.C.K., Liang, M.-C., Tsai, C.-J., Lin, F.-J., Chen, J.-P., Huang, Y.-T., 2012. Dust transport from non-East Asian sources to the North pacific. Geophys. Res. Lett. 39.

Hu, Z.Y., Huang, J.P., Zhao, C., Jin, Q.J., Ma, Y.Y., Yang, B., 2020. Modeling dust sources, transport, and radiative effects at different altitudes over the Tibetan Plateau. Atmos. Chem. Phys. 20, 1507–1529.

Huang, J., Fu, Q., Su, J., Tang, Q., Minnis, P., Hu, Y., Yi, Y., Zhao, Q., 2009. Taklimakan dust aerosol radiative heating derived from CALIPSO observations using the Fu-Liou radiation model with CERES constraints. Atmos. Chem. Phys. 9, 4011–4021.

Huang, J., Lin, B., Minnis, P., Wang, T., Wang, X., Hu, Y., Yi, Y., Ayers, J.K., 2006. Satellite-based assessment of possible dust aerosols semi-direct effect on cloud water path over East Asia. Geophys. Res. Lett. 33.

Huang, J., Minnis, P., Chen, B., Huang, Z., Liu, Z., Zhao, Q., Yi, Y., Ayers, J.K., 2008. Long-range transport and vertical structure of Asian dust from CALIPSO and surface measurements during PACDEX. J. Geophys. Res. Atmos. 113.

Huang, J.P., Wang, T.H., Wang, W.C., Li, Z.Q., Yan, H.R., 2014. Climate effects of dust aerosols over East Asian arid and semiarid regions. J. Geophys. Res. Atmos. 119, 11398–11416.

Huang, Z., Huang, J., Hayasaka, T., Wang, S., Zhou, T., Jin, H., 2015. Short-cut transport path for Asian dust directly to the Arctic: a case study. Environ. Res. Lett. 10.

Iacono, M.J., Delamere, J.S., Mlawer, E.J., Shephard, M.W., Clough, S.A., Collins, W.D., 2008. Radiative forcing by long-lived greenhouse gases: calculations with the AER radiative transfer models. J. Geophys. Res. Atmos. 113.

Iwasaka, Y., Shibata, T., Nagatani, T., Shi, G.Y., Kim, Y.S., Matsuki, A., Trochkine, D., Zhang, D., Yamada, M., Nagatani, M., Nakata, H., Shen, Z., Li, G., Chen, B., Kawahira, K., 2003. Large depolarization ratio of free tropospheric aerosols over the Taklamakan Desert revealed by lidar measurements: possible diffusion and transport of dust particles. J. Geophys. Res. Atmos. 108.

Kawai, K., Kai, K., Jin, Y., Sugimoto, N., Batdorj, D., 2015. Dust event in the Gobi Desert on 22-23 may 2013: transport of dust from the atmospheric boundary layer to the free troposphere by a. Cold Front. Sola 11, 156–159.

Lee, H.N., Igarashi, Y., Chiba, M., Aoyama, M., Hirose, K., Tanaka, T., 2006. Global model simulations of the transport of asian and sahara dust: total deposition of dust mass in Japan. Water Air Soil Pollut. 169, 137–166.

Lee, Y.C., Yang, X., Wenig, M., 2010. Transport of dusts from East Asian and non-East Asian sources to Hong Kong during dust storm related events 1996-2007. Atmos. Environ. 44, 3728–3738.

Levy, R.C., Mattoo, S., Munchak, L.A., Remer, L.A., Sayer, A.M., Patadia, F., Hsu, N.C., 2013. The Collection 6 MODIS aerosol products over land and ocean. Atmos. Meas. Tech. 6, 2989–3034.

Li, Z., Niu, F., Fan, J., Liu, Y., Rosenfeld, D., Ding, Y., 2011. Long-term impacts of aerosols on the vertical development of clouds and precipitation. Nat. Geosci. 4, 888–894.

Liao, J., Zhou, T., Han, B., Huang, Z., Jianrong, B., 2023. Aerosol types discrimination in semi-arid region of Northwest China using ground-based lidar data. J. Arid Meteorol. 41, 570–578.

Liu, Q., Huang, Z., Hu, Z., Dong, Q., Li, S., 2022. Long-range transport and evolution of saharan dust over East Asia from 2007 to 2020. J. Geophys. Res. Atmos. 127.

Mahowald, N.M., Baker, A.R., Bergametti, G., Brooks, N., Duce, R.A., Jickells, T.D., Kubilay, N., Prospero, J.M., Tegen, I., 2005. Atmospheric global dust cycle and iron inputs to the ocean. Global Biogeochem. Cycles 19.

Mamouri, R.E., Ansmann, A., 2014. Fine and coarse dust separation with polarization lidar. Atmos. Meas. Tech. 7, 3717–3735.

Mamouri, R.E., Ansmann, A., 2017. Potential of polarization/Raman lidar to separate fine dust, coarse dust, maritime, and anthropogenic aerosol profiles. Atmos. Meas. Tech. 10, 3403–3427.

Meng, L., Yang, X., Zhao, T., He, Q., Lu, H., Mamtimin, A., Huo, W., Yang, F., Liu, C., 2019. Modeling study on three-dimensional distribution of dust aerosols during a dust storm over the Tarim Basin, Northwest China. Atmos. Res. 218, 285–295.

Minamoto, Y., Nakamura, K., Wang, M., Kawai, K., Ohara, K., Noda, J., Davaanyam, E., Sugimoto, N., Kai, K., 2018. Large-scale dust event in East Asia in may 2017: dust emission and transport from multiple source regions. Inside Solaris 14, 33–38.

Morman, S.A., Plumlee, G.S., 2013. The role of airborne mineral dusts in human disease. Aeolian Res. 9, 203–212.

Olauson, J., 2018. ERA5: the new champion of wind power modelling? Renew. Energy 126, 322–331.

Pan, X., Uno, I., Wang, Z., Nishizawa, T., Sugimoto, N., Yamamoto, S., Kobayashi, H., Sun, Y., Fu, P., Tang, X., Wang, Z., 2017. Real-time observational evidence of changing Asian dust morphology with the mixing of heavy anthropogenic pollution. Sci. Rep. 7.

Park, C.B., Sugimoto, N., Matsui, I., Shimizu, A., Tatarov, B., Kamei, A., Lee, C.H., Uno, I., Takemura, T., Westphal, D.L., 2005. Long-range transport of saharan dust to East Asia observed with lidars. Inside Solaris 1, 121–124.

Patashnick, H., Rupprecht, E.G., 1991. Continuous PM-10 measurements using the tapered element oscillating microbalance. J. Air Waste Manag. Assoc. 41, 1079–1083.

Prospero, J.M., Delany, A.C., Delany, A.C., Carlson, T.N., 2021. The discovery of african dust transport to the western hemisphere and the saharan air layer. Bull. Am. Meteorol. Soc. 102, E1239–E1260.

Ruan, X.Y., Zhao, C., Zaveri, R.A., He, P.Z., Wang, X.M., Shao, J.Y., Geng, L., 2022. Simulations of aerosol pH in China using WRF-Chem (v4.0): sensitivities of aerosol pH and its temporal variations during haze episodes. Geosci. Model Dev. (GMD) 15, 6143–6164.

Schroedter-Homscheidt, M., Oumbe, A., Benedetti, A., Morcrette, J.J., 2013. Aerosols for concentrating solar electricity production forecasts: requirement quantification and ECMWF/MACC aerosol forecast assessment. Bull. Am. Meteorol. Soc. 94, 903–914.

Seinfeld, J.H., Bretherton, C., Carslaw, K.S., Coe, H., DeMott, P.J., Dunlea, E.J., Feingold, G., Ghan, S., Guenther, A.B., Kahn, R., Kraucunas, I., Kreidenweis, S.M., Molina, M.J., Nenes, A., Penner, J.E., Prather, K.A., Ramanathan, V., Ramaswamy, V., Rasch, P.J., Ravishankara, A.R., Rosenfeld, D., Stephens, G., Wood, R., 2016. Improving our fundamental understanding of the role of aerosol-cloud interactions in the climate system. Proc. Natl. Acad. Sci. U.S.A. 113, 5781–5790.

Stein, A.F., Draxler, R.R., Rolph, G.D., Stunder, B.J.B., Cohen, M.D., Ngan, F., 2015. NOAA'S HYSPLIT atmospheric transport and dispersion modeling system. Bull. Am. Meteorol. Soc. 96, 2059–2077.

Sugimoto, N., Jin, Y., Shimizu, A., Nishizawa, T., Yumimoto, K., 2019a. Transport of mineral dust from Africa and Middle East to East Asia observed with the lidar network (AD-Net). Inside Solaris 15, 257–261.

Sugimoto, N., Shimizu, A., Nishizawa, T., Jin, Y., 2019b. Long-range transport of mineral dust observed with the Asian Dust and aerosol lidar observation Network (AD-Net). E3S Web Conf. 99, 02001 (02008 pp.)-02001 (02008 pp.).

Sugimoto, N., Shimizu, A., Nishizawa, T., Jin, Y., Yumimoto, K., 2019c. LONG-RANGE-TRANSPORTED mineral dust from africa and MIDDLE EAST to East Asia observed with the asian dust and aerosol lidar observation network (AD-NET). In: 29th International Laser Radar Conference (ILRC), Hefei, PEOPLES R CHINA.

Tanaka, T.Y., Chiba, M., 2006. A numerical study of the contributions of dust source regions to the global dust budget. Global Planet. Change 52, 88–104.

Tanaka, T.Y., Kurosaki, Y., Chiba, M., Matsumura, T., Nagai, T., Yamazaki, A., Uchiyama, A., Tsunematsu, N., Kai, K., 2005. Possible transcontinental dust transport from North Africa and the Middle East to East Asia. Atmos. Environ. 39, 3901–3909.

Tazaki, K., Wakimoto, R., Minami, Y., Yamamoto, M., Miyata, K., Sato, K., Saji, I., Chaerun, S.K., Zhou, G.P., Morishita, T., Asada, R., Segawa, H., Imanishi, H., Kato, R., Otani, Y., Watanabe, T., 2004. Transport of carbon-bearing dusts from Iraq to Japan during Iraq's war. Atmos. Environ. 38, 2091–2109.

Thompson, G., Eidhammer, T., 2014. A study of aerosol impacts on clouds and precipitation development in a large winter cyclone. J. Atmos. Sci. 71, 3636–3658.

Twomey, S., 1991. AEROSOLS, clouds and radiation. Atmos. Environ., Part A 25, 2435–2442.

Uno, I., Eguchi, K., Yumimoto, K., Takemura, T., Shimizu, A., Uematsu, M., Liu, Z., Wang, Z., Hara, Y., Sugimoto, N., 2009. Asian dust transported one full circuit around the globe. Nat. Geosci. 2, 557–560.

Wang, H., Li, Z., Goloub, P., Hu, Q., Wang, F., Lv, Y., Ge, B., Hu, X., Shang, J., Zhang, P., 2022. Identification of Typical Dust Sources in Tarim Basin Based on Multi-Wavelength Raman Polarization Lidar. Atmospheric Environment, 119358.

Winker, D.M., Pelon, J., Coakley, J.A., Ackerman, S.A., Charlson, R.J., Colarco, P.R., et al., 2010. THE CALIPSO mission A global 3D view of aerosols and clouds. Bull. Am. Meteorol. Soc. 91, 1211–1229.

Xie, H.L., Zhou, T., Fu, Q., Huang, J.P., Huang, Z.W., Bi, J.R., Shi, J.S., Zhang, B.D., Ge, J. M., 2017. Automated detection of cloud and aerosol features with SACOL micro-pulse lidar in northwest China. Opt Express 25, 30732–30753.

Xu, X., Zhao, P., Yin, Y., Cheng, W., Wang, J., Li, P., Liu, Y., Dai, J., Yuan, W., 2022. Dust particles transport during the rare strong sandstorm process in Northern China in early year 2021. Air Qual. Atmosph. Health 15, 929–936.

Yumimoto, K., Kajino, M., Tanaka, T.Y., Uno, I., 2019. Dust vortex in the Taklimakan Desert by himawari-8 high frequency and resolution observation. Sci. Rep. 9.

Zaveri, R.A., Easter, R.C., Fast, J.D., Peters, L.K., 2008. Model for simulating aerosol interactions and Chemistry (MOSAIC). J. Geophys. Res. Atmos. 113.

Zhao, C., Chen, S., Leung, L.R., Qian, Y., Kok, J.F., Zaveri, R.A., Huang, J., 2013a. Uncertainty in modeling dust mass balance and radiative forcing from size parameterization. Atmos. Chem. Phys. 13, 10733–10753.

Zhao, C., Leung, L.R., Easter, R., Hand, J., Avise, J., 2013b. Characterization of speciated aerosol direct radiative forcing over California. J. Geophys. Res. Atmos. 118, 2372–2388.

Zhou, C., Liu, Y., Zhu, Q., He, Q., Zhao, T., Yang, F., Huo, W., Yang, X., Mamtimin, A., 2022. In situ observation of warm atmospheric layer and the heat contribution of suspended dust over the Tarim Basin. Atmos. Chem. Phys. 22, 5195–5207.

Zhou, T., Huang, J.P., Huang, Z.W., Liu, J.J., Wang, W.C., Lin, L., 2013. The depolarization-attenuated backscatter relationship for dust plumes. Opt Express 21, 15195–15204.

Zhou, T., Xie, H.L., Bi, J.R., Huang, Z.W., Huang, J.P., Shi, J.S., Zhang, B.D., Zhang, W., 2018. Lidar measurements of dust aerosols during three field campaigns in 2010, 2011 and 2012 over northwestern China. Atmosphere 9.

Zhou, T., Xie, H.L., Jiang, T., Huang, J.P., Bi, J.R., Huang, Z.W., Shi, J.S., 2021. Seasonal characteristics of aerosol vertical structure and autumn enhancement of non-spherical particle over the semi-arid region of northwest China. Atmos. Environ. 244.

Zhou, X.W., Zhou, T., Fang, S.Y., Han, B.S., He, Q., 2023. Investigation of the vertical distribution characteristics and microphysical properties of summer mineral dust masses over the Taklimakan Desert using an unmanned aerial vehicle. Rem. Sens. 15, 3556.